CrossMark

Measuring the ^{34}S and ^{33}S Isotopic Ratios of Volatile Sulfur during Planet Formation

Alice S. Booth[1,12] , Maria N. Drozdovskaya[2] , Milou Temmink[3] , Hideko Nomura[4] , Ewine F. van Dishoeck[3,5] ,
Luke Keyte[6] , Charles J. Law[7,13] , Margot Leemker[3] , Nienke van der Marel[3] , Shota Notsu[8,9,10] , Karin Öberg[1] , and
Catherine Walsh[11]
[1] Center for Astrophysics | Harvard & Smithsonian, 60 Garden St., Cambridge, MA 02138, USA; alice.booth@cfa.harvard.edu
[2] Physikalisch-Meteorologisches Observatorium Davos und Weltstrahlungszentrum (PMOD/WRC), Dorfstrasse 33, CH-7260, Davos Dorf, Switzerland
[3] Leiden Observatory, Leiden University, 2300 RA Leiden, The Netherlands
[4] Division of Science, National Astronomical Observatory of Japan, 2-21-1 Osawa, Mitaka, Tokyo 181-8588, Japan
[5] Max-Planck-Institut fúr Extraterrestrische Physik, Giessenbachstrasse 1, 85748 Garching, Germany
[6] Department of Physics and Astronomy, University College London, Gower Street, London, WC1E 6BT, UK
[7] Department of Astronomy, University of Virginia, Charlottesville, VA 22904, USA
[8] Department of Earth and Planetary Science, Graduate School of Science, The University of Tokyo, 7-3-1 Hongo, Bunkyo-ku, Tokyo 113-0033, Japan
[9] Department of Astronomy, Graduate School of Science, The University of Tokyo, 7-3-1 Hongo, Bunkyo-ku, Tokyo 113-0033, Japan
[10] Star and Planet Formation Laboratory, RIKEN Cluster for Pioneering Research, 2-1 Hirosawa, Wako, Saitama 351-0198, Japan
[11] School of Physics and Astronomy, University of Leeds, Leeds LS2 9JT, UK

Abstract

Stable isotopic ratios constitute powerful tools for unraveling the thermal and irradiation history of volatiles. In particular, we can use our knowledge of the isotopic fractionation processes active during the various stages of star, disk, and planet formation to infer the origins of different volatiles with measured isotopic patterns in our own solar system. Observations of planet-forming disks with the Atacama Large Millimeter/submillimeter Array (ALMA) now readily detect the heavier isotopologues of C, O, and N, while the isotopologue abundances and isotopic fractionation mechanisms of sulfur species are less well understood. Using ALMA observations of the SO and SO$_2$ isotopologues in the nearby, molecule-rich disk around the young star Oph-IRS 48 we present the first constraints on the combined ^{32}S/^{34}S and ^{32}S/^{33}S isotope ratios in a planet-forming disk. Given that these isotopologues likely originate in relatively warm gas (>50 K), like most other Oph-IRS 48 volatiles, SO is depleted in heavy sulfur, while SO$_2$ is enriched compared to solar system values. However, we cannot completely rule out a cooler gas reservoir, which would put the SO sulfur ratios more in line with comets and other solar system bodies. We also constrain the S^{18}O/SO ratio and find the limit to be consistent with solar system values given a temperature of 60 K. Together these observations show that we should not assume solar isotopic values for disk sulfur reservoirs, but additional observations are needed to determine the chemical origin of the abundant SO in this disk, inform on what isotopic fractionation mechanism(s) are at play, and aid in unraveling the history of the sulfur budget during the different stages of planet formation.

Unified Astronomy Thesaurus concepts: Protoplanetary disks (1300); Astrochemistry (75); Isotopic abundances (867); Small Solar System bodies (1469); Submillimeter astronomy (1647)

1. Introduction

The volatile building blocks of planets, moons, and comets exist as gas and ice in protoplanetary disks, which in turn have an origin as ices in cold, dark, molecular clouds (e.g., K. I. Öberg & E. A. Bergin 2021). On million-year timescales, the material in the disk is subject to a variety of physical and chemical processes that can alter this initially inherited volatile reservoir (e.g., Y. Aikawa et al. 2022). The isotopic ratios of volatile elements can be used as tools to unravel the history of this material throughout the different stages of the star, disk, and planet formation. The main drivers of isotopic fractionation are low-temperature chemical reactions, due to the differences in the zero-point vibrational energies of different isotopologues, and isotope-selective photodissociation (see H. Nomura et al. 2023 for a recent review).

From submillimeter observations of planet-forming disks we now have detections of simple molecules containing the heavier isotopes D, ^{13}C, ^{18}O, ^{17}O, ^{15}N, and ^{34}S (summarized in K. I. Öberg et al. 2023). One of the most readily detected isotopes in disks is deuterium, and the measured enhancement of D/H in simple molecules (e.g., HCN, HCO$^+$, and N$_2$H$^+$) can be explained via in situ isotope exchange reactions that are active in the cold outer disk (e.g., C. Favre et al. 2015; Y. Aikawa et al. 2018; G. Cataldi et al. 2021; C. E. Muñoz-Romero et al. 2023). The ^{14}N/^{15}N ratio has also been measured in disks for both HCN and CN, where fractionation can likely be attributed to the isotope-selective photodissociation of N$_2$ in the disk atmosphere (A. N. Heays et al. 2014; P. Hily-Blant et al. 2017, 2019; V. V. Guzmán et al. 2017; R. Visser et al. 2018). Although C^{18}O is readily detectable in nearby disks, the optical depth of the line typically prevents a measurement of the oxygen isotope ratio from CO observations alone. Recent work from K. Furuya et al. (2022) shows that optically thin HCO$^+$ isotopologue lines can give access to the ^{16}O/^{18}O ratio in disks, which can be used to test mechanisms for recovering

Table 1
Molecular Line and Image Properties Where Molecular Transition Data Are Taken from CDMS (H. S. P. Müller et al. 2005; C. P. Endres et al. 2016)

Mol.	Transition	Frequency (GHz)	E_{up} (K)	$\log_{10}(A_{\mathrm{ul}})$ (s^{-1})	Beam (Position Angle) (arcsec × arcsec (deg))	Peak Integrated Intensity (mJy beam^{-1} km s^{-1})	Uncertainty (mJy beam^{-1} km s^{-1})
SO	$J = 3_3 - 3_2$	339.3414590	25.5	−4.8372	0.34 × 0.28 (88)	56.2	4.7
^{34}SO	$J = 8_8 - 7_7$	339.8572694	77.3	−3.2944	0.34 × 0.27 (88)	58.7	4.7
^{34}SO	$J = 9_8 - 8_7$	337.5801467	86.1	−3.3109	0.34 × 0.28 (−89)	52.1	5.2
^{33}SO[a]	$J = 7_8 - 6_7$	337.1986199	80.5	−3.3158	0.34 × 0.28 (−90)	22.9	5.3
^{33}SO[a]	$J = 9_8 - 8_7$	343.0882949	78.0	−3.2819	0.34 × 0.27 (−85)	29.5	4.7
S^{18}O	$J = 8_9 - 7_8$	355.5735893	93.1	−3.2414	0.33 × 0.26 (−85)	3.6	0.9
SO$_2$	$J = 6_{4,2} - 6_{3,3}$	357.9258478	58.6	−3.5845	0.33 × 0.26 (−85)	50.1	5.9
^{34}SO$_2$	$J = 6_{3,3} - 5_{2,4}$	362.1582327	40.7	−3.4839	0.53 × 0.42 (80)	46.5	5.0

Note.
[a] The ^{33}SO lines are blends of multiple hyperfine components. Here, we show the properties of the strongest transition, and the flux is the total of the blended lines. The $J = 7_8 - 6_7$ line includes the F = 17/2 − 15/2, F = 15/2 − 13/2, F = 11/2 − 9/2, and F = 11/2 − 9/2 hyperfine components, and the $J = 9_8 - 8_7$ line includes the F = 21/2 − 19/2, F = 19/2 − 17/2, F = 17/2 − 15/2, and F = 15/2 − 13/2 hyperfine components.

the oxygen isotope fractionation observed in the solar system (B. Marty 2012). In the specific case of the TW Hya disk, the relative abundance of ^{18}O is found to be consistent with the local interstellar medium (ISM) value, i.e., it is not enhanced or depleted in the disk gas (K. Furuya et al. 2022).

Overall, the results for Class II disks so far do not require the inheritance of fractionated material from the cold cloud stage. The least understood of the detected volatile elements in disks is sulfur, where both its primary volatile form on the ice and the expected isotopic ratios due to thermal and photoprocessing are unclear. The rarer isotopologues of CS, C^{34}S, and ^{13}CS, have been detected in a handful of disks, but we lack concrete information on potential in situ or inherited isotope fractionation processes that may have occurred (R. Le Gal et al. 2019, 2021; R. A. Loomis et al. 2020; N. T. Phuong et al. 2021; A. S. Booth et al. 2023). However, when considering comets, the remnant icy material from the protoplanetary disk that formed our solar system, we have significantly more information. The isotopic ratios in sulfur-bearing molecules have been well measured in comet 67P/Churyumov–Gerasimenko (67P/C-G), and there are indicators that isotopic fractionation processes have occurred (J. A. Paquette et al. 2017; U. Calmonte et al. 2017; K. Altwegg et al. 2020). In particular, both the ^{32}S/^{34}S and ^{32}S/^{33}S ratios have been derived for a collection of simple molecules, and these measurements trace a bulk depletion of heavier isotopes relative to solar system standards that cannot be explained by photodissociation (U. Calmonte et al. 2017). Additionally, the simple S-bearing molecules SO, SO$_2$, and OCS are all enhanced in ^{18}O by approximately a factor of 2 relative to solar (K. Altwegg et al. 2020), and HDS/H$_2$S is well above the interstellar elemental ratio (K. Altwegg et al. 2017). The cometary dust particles on the other hand have a ^{32}S/^{34}S ratio consistent with the expected terrestrial value (J. A. Paquette et al. 2017).

The disk with the most observed volatile sulfur, and therefore the source with the most promise for measuring isotopic ratios of sulfur, is the Oph-IRS 48 disk. Oph-IRS 48 is a nearby (135 pc), young Herbig Ae star (J. M. Brown et al. 2012; Gaia Collaboration et al. 2018) host to a molecule-rich transition disk with an asymmetric dust trap where both, SO and SO$_2$ have been robustly detected (A. S. Booth et al. 2021; A. Booth et al. 2024). The observable chemistry in this disk appears to be dominated by the sublimation of ices indicated by the presence of CH$_3$OH and other complex organic molecules in the gas phase (N. van der Marel et al. 2021; N. G. C. Brunken et al. 2022; A. Booth et al. 2024). This makes the Oph-IRS 48 disk a powerful observational

laboratory to investigate the isotopic makeup of the typically hidden icy reservoir in disks. Here, we provide the first measurements of the combined ^{32}S/^{34}S and ^{32}S/^{33}S ratios in a planet-forming disk. We also report a stringent upper limit on the S^{18}O abundance and use this to estimate the corresponding lower limit of the ^{16}O/^{18}O isotopic ratio.

2. Methods

We use molecular line observations of the Oph-IRS 48 planet-forming disk taken with the Atacama Large Millimeter/sub-millimeter Array (ALMA) from the programs 2017.1.00834.S (PI: Adriana Pohl) and 2021.1.00738.S (PI: Alice S. Booth). The former were first presented in N. van der Marel et al. (2021) and A. S. Booth et al. (2021) and the latter in A. Booth et al. (2024). The 2017.1.00834.S data were pipeline calibrated by S. Ohashi et al. (2020), and A. S. Booth et al. (2021) imaged these data with CASA task tCLEAN (J. P. McMullin et al. 2007) at a velocity resolution of 1.7 km s^{-1} and a Briggs robust weighting of 0.5 resulting in a ≈0.″45 beam. The 2021.1.00738.S data were self-calibrated (both phase and amplitude) and imaged with CASA task tCLEAN at a velocity resolution of 0.9 km s^{-1} with a Briggs robust weighting of 0.5 resulting in a ≈0.″3 beam (N. van der Marel et al. 2021). All integrated intensity maps were generated using Keplerian masks (R. Teague 2020). In the above referenced works, the data calibration, line identification, and imaging steps are described in full detail.

The focus of this paper is on the sulfur-bearing molecules covered in the data. A. S. Booth et al. (2021) and A. Booth et al. (2024) report the detections of SO, ^{34}SO, ^{33}SO, SO$_2$, and ^{34}SO$_2$, and we use the integrated intensity maps from these works. One transition of S^{18}O with a $A_{\mathrm{ul}} \approx 10^{-3.2}$ s^{-1} is covered in the data from A. Booth et al. (2024), and we tentatively detect this line in one velocity channel (0.9 km s^{-1}) at a signal-to-noise ratio of 4. Although only detected in one channel, this is the same velocity channel where the main SO isotope lines are the brightest, and the local line width per pixel is only ≈2–3 km s^{-1}. A robust detection would require 3σ emission over >3 channels to confirm. We therefore consider this as an upper limit on the S^{18}O abundance in this disk. The channel maps of the S^{18}O line are shown in Figure A1. This S^{18}O line was imaged in the same manner as the other lines from A. Booth et al. (2024) and is part of the same ALMA data set. Table 1 lists the properties of the transitions and images presented in this paper.
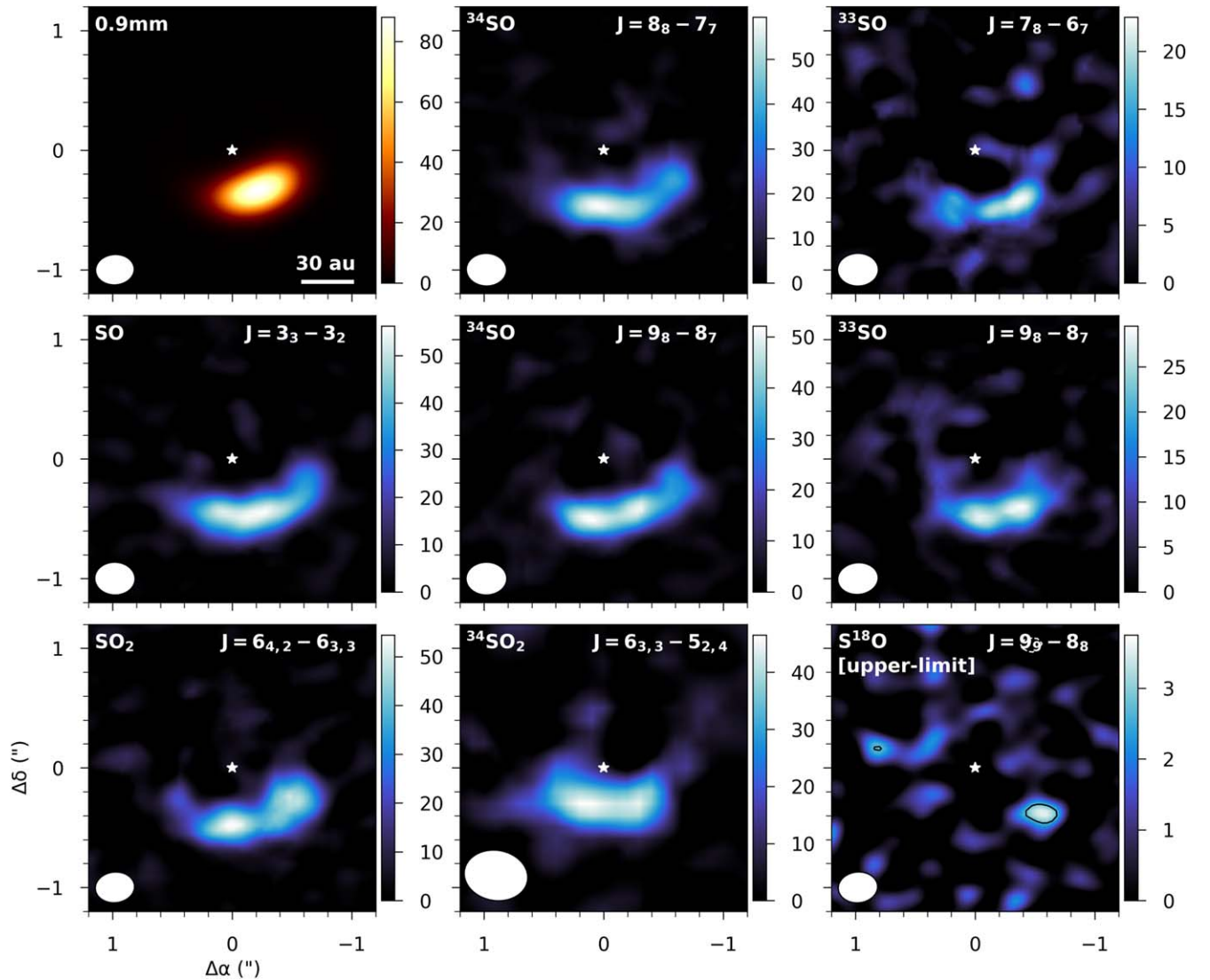
Figure 1. Integrated intensity maps of the 0.9 mm dust continuum emission and the sulfur isotopologues in the Oph-IRS 48 disk. The units of the color bar are mJy beam^{-1} km s^{-1} for the molecular lines and mJy beam^{-1} for the continuum. The black contours on the S^{18}O map highlight 3× the rms noise level.

Under the typical assumptions of optically thin line emission and local thermodynamic equilibrium (as done by R. A. Loomis et al. 2018), we estimate the peak column density traced by the SO and SO$_2$ isotopologues detected in the Oph-IRS 48 disk. The various line properties and partition functions of each isotopologue are taken from the Cologne Database for Molecular Spectroscopy (H. S. P. Müller et al. 2001, 2005; C. P. Endres et al. 2016) with data from F. J. Lovas (1985), F. J. Lovas et al. (1992), and T. Klaus et al. (1996). The errors in the peak column densities are propagated from the errors in the integrated intensity maps (as listed in Table 1) where these errors are a measure of the rms noise of the line-free regions of the images without Keplerian masking. The rms in the S^{18}O is lower than the other lines since this integrated map is only calculated for one channel.

We calculate these column densities at a range of excitation temperatures (30–150 K in steps of 10 K) that cover the range of expected excitation conditions in this disk. The lower limit of this range is informed by the brightness temperature of the midplane millimeter dust, which is at a minimum of 30 K, and the upper limit is from the ≳100 K brightness temperature of

the optically thick CO isotopologues, which trace the disk surface layers (N. van der Marel et al. 2021; M. Leemker et al. 2023) and the rotational temperatures of H$_2$CO, CH$_3$OH, and SO$_2$ (N. van der Marel et al. 2021 and M. Temmink et al. 2024, in preparation). In particular, using the line survey data of the Oph-IRS 48 disk presented in A. Booth et al. (2024), where >10 SO$_2$ lines are detected with an upper energy level range of 35–200 K, M. Temmink et al. (2024, in preparation) find the rotational temperature for SO$_2$ to be very well constrained to ≈60 K at the emission peak. As the SO and SO$_2$ emission is cospatial in the observations (as shown in Figure 1) and chemically linked in disk models through their origins in the warm molecular layer and not the disk midplane (e.g., L. Keyte et al. 2024), we expect them to trace the same gas temperature. Additionally, to support this assumption of warm gas in disk models, SO and SO$_2$ freeze out at dust temperatures less than ≈40 and ≈60 K, respectively (e.g., D. Semenov et al. 2018). We note that this will depend on the assumed binding energies; for example, J. Perrero et al. (2021) used quantum chemical calculations to show that SO has a range of binding energies on a water ice cluster (60 molecules), spanning a temperature

Table 2
Derived Peak Column Densities and Isotope Ratios with Associated 1σ Errors

Molecule	N_{peak} (cm^{-2})		
	T_{ex}: 30 K	**60 K**	100 K
^{32}SO	$2.7 \pm 0.2 \times 10^{15}$	$3.6 \pm 0.3 \times 10^{15}$	$5.1 \pm 0.41 \times 10^{15}$
^{34}SO	$2.0 \pm 0.2 \times 10^{14}$	$1.0 \pm 0.1 \times 10^{14}$	$1.0 \pm 0.09 \times 10^{14}$
^{33}SO	$2.2 \pm 0.4 \times 10^{13}$	$1.2 \pm 0.2 \times 10^{13}$	$1.3 \pm 0.25 \times 10^{13}$
S^{18}O	$1.5 \pm 0.4 \times 10^{13}$	$0.7 \pm 0.2 \times 10^{13}$	$0.7 \pm 0.17 \times 10^{13}$
SO$_2$	$6.9 \pm 0.4 \times 10^{14}$	$6.7 \pm 0.5 \times 10^{14}$	$9.6 \pm 0.69 \times 10^{14}$
^{34}SO$_2$	$0.9 \pm 0.1 \times 10^{14}$	$1.3 \pm 0.1 \times 10^{14}$	$2.1 \pm 0.21 \times 10^{14}$

Ratio	T_{ex}: 30 K	**60 K**	100 K	V-CDT
^{32}SO/^{34}SO	13 ± 1	34 ± 4.0	50 ± 6.0	22.64
^{32}SO$_2$/^{34}SO$_2$	7.5 ± 0.9	5.2 ± 0.6	4.6 ± 0.6	22.64
^{32}SO/^{33}SO	120 ± 25	290 ± 60	410 ± 90	126.9
^{32}SO/S^{18}O	>180	>500	>760	498.7

Deviation from V-CDT	T_{ex}: 30 K	**60 K**	100 K	...
δ^{34}SO	690^{+160}_{-200}	-340^{+90}_{-70}	-550^{+60}_{-50}	...
δ^{34}SO$_2$	2016^{+410}_{-320}	3350^{+250}_{-170}	3920^{+740}_{-570}	...
δ^{33}SO	23^{+250}_{-170}	-559^{+120}_{-80}	-690^{+80}_{-60}	...
δS^{18}O	<1820	<5	<-340	...

Note. Note that in bold text we highlight our fiducial temperature. The V-CDT standard values are from T. Ding et al. (2001) and R. A. Werner & W. A. Brand (2001).

range of 933–3483 K with an average value of 2128 K, which is lower than the values listed in UDfA and KIDA (2800 and 2600 K, respectively). Ideally, we would have an independent measure of the SO rotational temperature, but in total, A. Booth et al. (2024) detect only three SO lines in the Oph-IRS 48 disk, and the high line opacities of the $J = 7_8 - 6_7$ and $J = 8_8 - 7_7$ transitions do not allow for a rotation diagram analysis. In this work, we only use the optically thinnest transition detected ($J = 3_3 - 3_2$) as a measure of the SO column density. For ^{34}SO and ^{33}SO two lines of each are detected, and we take the average column density traced by these lines at each temperature. Therefore, although we expect the SO to trace warm 60 K gas, we cannot make an independent temperature measurement to confirm this; therefore, we explore a range of higher and lower gas temperatures to see how sensitive the inferred isotopic ratios is to this assumption. Due to the different intrinsic properties of the transitions of each isotopologue these ratios will vary with the assumed gas temperature.

To compare our isotope ratios with measurements of isotopic variations in solar system bodies, we also calculate the deviation of our ratios relative to the Vienna Canyon Diablo Troilite (V-CDT). This is the most common isotopic standard used in comet and meteorite studies. The standard ratios used are 22.64 for ^{32}S/^{34}S, 126.9 for ^{32}S/^{33}S, and 498.7 for ^{16}O/^{18}O (R. A. Werner & W. A. Brand 2001; T. Ding et al. 2001). These differ slightly from the local ISM ratios, where in particular, ^{16}O/^{18}O is 550 (T. L. Wilson & R. Rood 1994). The deviations (δ) are reported in units of per mille (‰) and are calculated as follows:

$$\delta^{34}\text{S} = [(^{34}\text{S}/^{32}\text{S})_{\text{disk}}/(^{34}\text{S}/^{32}\text{S})_{\text{standard}} - 1] \times 1000,$$

where the above is an example for the ^{34}S/^{32}S ratio.

3. Results

In Figure 1, we present the integrated intensity maps of sulfur isotopologues in the Oph IRS 48 disk and the 0.9 mm

continuum emission. The molecular species all appear cospatial and are only present in the southern region of the disk, where the millimeter dust grains are most prominent. From these integrated intensity maps, we take the peak integrated flux and use this to calculate the molecular column density traced by each of the isotopologues. The resulting peak column densities, corresponding isotopic ratios, and deviations from V-CDT at 30, 60, and 100 K are listed in Table 2 and across the full temperature range in Figure 2. We also compared these peak column densities to the averaged column densities derived from the whole SO- and SO$_2$-emitting region and find that the resulting isotope ratios, the key result of this paper, are within the quoted 1σ errors.

In Figure B1, we show the inferred ratios as a function of the assumed temperature. The isotope ratios derived from ^{32}SO all increase with increasing gas temperature, and both ^{34}S and ^{33}S are consistent with the V-CDT values at temperatures lower than ≈ 50 K. When adopting our fiducial temperature of 60 K, we find that traced in SO line emission, the Oph-IRS 48 disk is depleted in both ^{34}S and ^{33}S with ^{32}S/^{34}S $= 34 \pm 4$ and ^{32}S/^{33}S $= 290 \pm 60$. The ^{16}O/^{18}O lower limit from SO of >500 is consistent with the V-CDT value. The SO $J = 3_3 - 3_2$ transition is optically thin with $\tau \approx 0.1$, and since the rare isotopes of SO are depleted relative to this, optical depth cannot explain the anomalous isotope ratios we recover when assuming our fiducial temperature of 60 K or a temperature above this. Additionally, the ^{34}SO/^{33}SO ratio is approximately constant with temperature and is always 40%–50% above the V-CDT value.

The SO$_2$ isotope ratios vary less with temperature, since the upper energy levels of the SO$_2$ and ^{34}SO$_2$ lines are similar. In contrast to our findings for SO, the ^{34}S column density appears to be enhanced at all temperatures when measured from the SO$_2$ and at 60 K the ^{32}S/^{34}S $= 5$. From a rotation diagram analysis, M. Temmink et al. (2024, in preparation) show that ^{32}SO$_2$ emission is optically thin, but because the observations are spatially and kinematically unresolved, the optical is
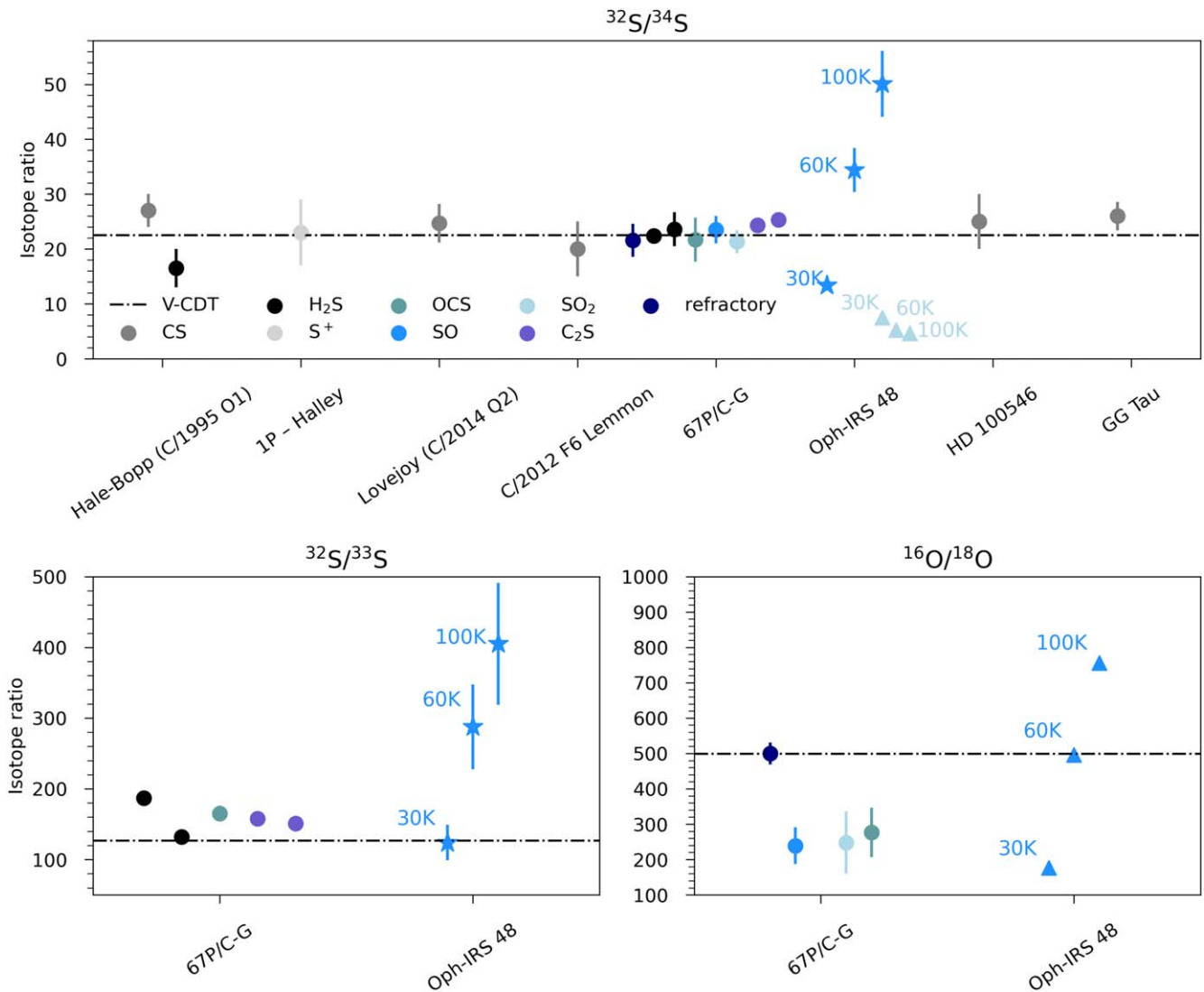
Figure 2. Inferred isotopic ratios of S and O in different volatile sulfur species detected toward comets and protoplanetary disks. The results for Oph-IRS 48 are highlighted by the star or arrow markers at temperatures of 30, 60, and 100 K. Note the ^{34}S ratio from SO_2 and the ^{18}O ratio from SO are lower limits. The dashed lines denote the V-CDT standard isotopic ratios for ^{32}S/^{34}S, ^{32}S/^{33}S, and ^{16}O/^{18}O (R. A. Werner & W. A. Brand 2001; T. Ding et al. 2001). The vertical bars mark the $\pm 1\sigma$ errors. The other disk values are taken from R. Le Gal et al. (2019), N. T. Phuong et al. (2021), and A. Booth et al. (2024). Cometary values are taken from D. C. Jewitt et al. (1997), J. A. Paquette et al. (2018), and K. Altwegg et al. (2020), as well as J. Crovisier et al. (2004), N. Biver et al. (2016), J. A. Paquette et al. (2017), and U. Calmonte et al. (2017). We exclude the S_2 isotope ratio reported in U. M. Calmonte (2015) and subsequently in J. A. Paquette et al. (2017) for 67P/C-G from our comparison due to the low signal to noise of the S_2 peak in the mass spectra and the significant contamination from other overlapping species (M. Rubin 2024, private communication).

likely underestimated. Therefore, the inferred ^{32}S/^{34}S ratio from SO_2 may only be a lower limit.

4. Discussion

The currently observed volatile sulfur reservoir in the Oph-IRS 48 disk is primarily in the form of SO. This is different to most Class II disks, where generally CS is the most common S-species detected (e.g., R. Le Gal et al. 2019, 2021). CS is detected in the Oph-IRS 48 disk, but its column density is $\approx 1000\times$ lower than for SO; therefore, CS makes a negligible contribution to the total S abundance (A. Booth et al. 2024). In Figure 3, we show the contributions from H_2S, S, OCS, SO, and SO_2 to the currently total observed volatile sulfur reservoirs in the low-mass embedded Class 0 protostar IRAS 16293-2442 B, the more evolved Class II disk Oph-IRS 48, the comet 67P/C-G, and the shocked region L1157-B1 (with

values from U. Calmonte et al. 2016; M. N. Drozdovskaya et al. 2018; J. Holdship et al. 2019; T. Kushwahaa et al. 2023; A. Booth et al. 2024).

The differences in sulfur reservoirs between IRAS 16293-2442 B and 67P/C-G are discussed in detail in M. N. Drozdovskaya et al. (2018), who suggest that UV irradiation during the star formation process converted H_2S to OCS. OCS is not detected in Oph-IRS 48 down to <1% of the SO column density, and this is unexpected, as discussed in A. Booth et al. (2024), due to the other signatures of ice sublimation in this disk. Interestingly, the SO_2/OCS ratio we see in Oph-IRS 48 is also significantly higher than that measured for the outbursting source V883 Ori, where ice sublimation is also occurring (Y. Yamato et al. 2024). Oph-IRS 48 is a young Herbig Ae star, and therefore the volatiles in the gas and ice phases will be subjected to UV irradiation, which could chemically transform the primary S-reservoir in the disk. It is also possible that in the
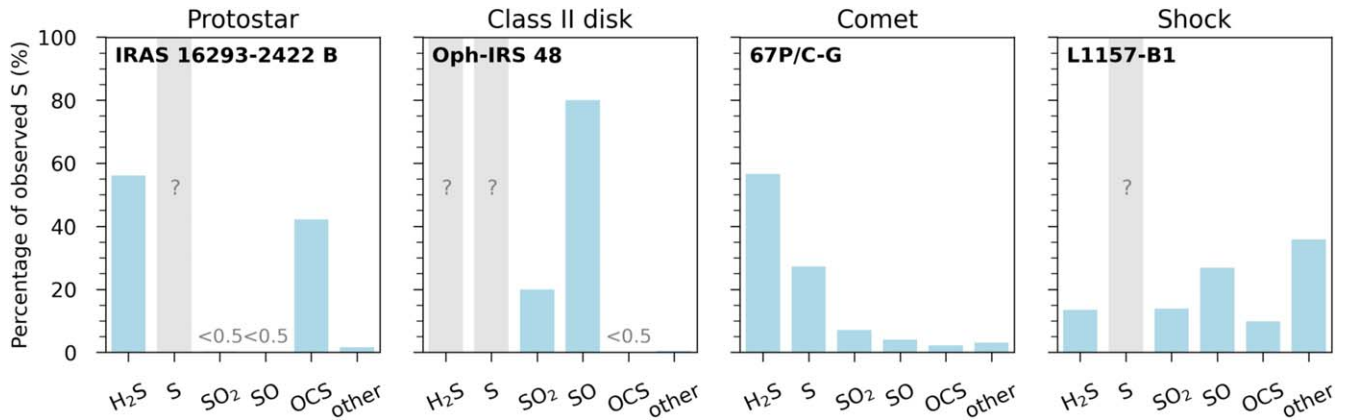
Figure 3. Bar plots showing the percentage of observed gas-phase sulfur in different atoms/molecules for the protostar IRAS 16293-2442 B, Class II disk Oph-IRS 48, comet 67P/C-G, and shocked region L1157-B1. Values are taken from U. Calmonte et al. (2016), M. N. Drozdovskaya et al. (2018), J. Holdship et al. (2019), T. Kushwahaa et al. (2023), and A. Booth et al. (2024). Where the percentage is less than 0.5%, a note is added. We note that this comparison naively assumes that 100% of the volatile S can be accounted for in the currently detected molecules in these systems.

Oph-IRS 48 disk there are shocks liberating a more refractory form of sulfur, e.g., S_2, that when released from the grains goes on to form SO (and SO_2) efficiently in the gas phase (as discussed in L. Keyte et al. 2024). Indeed, the bulk of the S in disks is expected to be in refractory form (M. Kama et al. 2019). The high SO/SO_2 ratio in Oph-IRS 48 is also most closely a match with that in the shocked region L1157-B1, but the CS/SO ratio is orders of magnitude higher in the shocked region when compared to the Oph-IRS 48 disk (J. Holdship et al. 2019). Observations of the shock tracer SiO (and SiS; C. J. Law et al. 2023) and key sulfur species H_2S will help unravel the distinctions between the volatile reservoir in the Oph-IRS 48 disk and that in other environments.

Given the differences in molecular reservoirs of S we may expect differences in the isotopic ratios on volatile sulfur in the Oph-IRS48 disk. To place our isotopic ratios in context, in Figure 2, we show a comparison of the isotope ratios measured in comets to Class II disks for a variety of simple species. The ratios we measure do vary as a function of the assumed gas temperature (as shown in Figures 2 and B1). If the gas is cool (<50 K), the ^{34}S and ^{33}S ratios for SO are within the 1–2σ range of the V-CDT values. This would mean there are no significant isotopic differences between the Oph-IRS 48 disk and the solar system and that volatile S is not severely fractionated during the planet formation timescale. Similarly, at 30 K we would tentatively recover the ^{18}O enhancement, as seen in 67P/C-G, but further data are needed to verify this.

The rotational temperature of SO_2 in this disk has been well constrained to be 60 K (M. Temmink et al. 2024, in preparation); therefore, we discuss the case where the SO gas is also warm, as also supported by astrochemical models (D. Semenov et al. 2018; L. Keyte et al. 2024). At temperatures of 60 K and above the isotope ratios for sulfur are anomalous when compared to the V-CDT and cometary values. This possible observed depletion of ^{34}S and ^{33}S traced in SO is currently not traced in any cometary volatiles and, in particular, not in the ^{34}SO measured in 67P/C-G (K. Altwegg et al. 2020). This depletion is also not traced in the refractory dust of 67P/C-G nor the dust collected in the STARDUST mission (P. R. Heck et al. 2012; J. A. Paquette et al. 2017). For the other few disks with robust measurements of ^{32}S/^{34}S from CS, these values are consistent with the expected isotope ratio of 22

(N. T. Phuong et al. 2021; A. Booth et al. 2024). In the broader context of meteorite samples, our δ^{34}S and δ^{33}S values, calculated at 60 K, lie at the most depleted end of the distribution of isotopic ratios measured in SiC grains from the meteorites Murchison and Indarch (this literature is summarized in U. Calmonte et al. 2017). The apparent factor ≈ 4 enhancement of ^{34}S in SO_2 is an extreme outlier in all cases, but this may be due to beam-diluted and optically thick $^{32}SO_2$ emission. This low ^{34}S ratio in SO_2 is similar to that measured in SO for Class 0/I sources in Perseus (E. Artur de la Villarmois et al. 2023), where this can be attributed to optically thick emission from the main isotopologue.

Finally, when considering the lower limit of the ^{18}O isotope ratio in SO at $\gtrsim 60$ K, we find a difference to the volatiles in 67P/C-G. The enhanced ^{18}O in SO, SO_2, and OCS in 67P/C-G and the high HDS/H_2S (of $\approx 10^{-3}$) indicate the possible presolar formation of these molecules in the cold dark cloud stage (K. Altwegg et al. 2017). In comparison, for warm gas, in the Oph-IRS 48 disk our upper limit does not indicate any oxygen isotope fractionation, similar to the findings from K. Furuya et al. (2022) for $H^{13}CO^+/HC^{18}O^+$ in TW Hya. The nominal ratio of ≈ 500 is also the same as that measured for the 67P/C-G cometary dust particles (J. A. Paquette et al. 2018).

The observations of Oph-IRS 48 show the possibility of isotopically distinct sulfur reservoirs in planet-forming disks with an isotopic fractionation distinct to that of 67P/C-G. The depletion of heavier isotopes and lack of ^{18}O enhancement would also suggest that low-temperature isotope exchange reactions are not responsible as these would have the opposite effect. If the optically thin nature of SO_2 holds, the different isotopic signatures in SO and SO_2 mean that they may not share a common formation path via H_2S and H_2O ice sublimation (D. Semenov et al. 2018; A. S. Booth et al. 2021). If SO and SO_2 both form from photodissociated H_2S, they would be expected to have the same isotopic ratios. The isotope-selective photodissociation of H_2S has been proposed as a mechanism for the enrichment of heavy isotopes in some chondritic meteorites, but if this were the case in Oph-IRS 48, we would expect both the SO and SO_2 to be enriched in the heavier isotopes, if they indeed formed from H_2S (S. Chakraborty et al. 2013; J. Labidi et al. 2017; L. G. Vacher et al. 2021). If there are shocks in the Oph-IRS 48 disk, the injection of refractory S into the gas phase could pollute the isotopic

ratios set by photoprocesses. Future observations of Oph-IRS 48 to detect H_2S and measure its isotopic ratios will be necessary to determine if SO and/or SO_2 are daughter molecules forming from H_2S. Additionally, observations of multiple optically thin lines of SO and its isotopologues will enable an independent temperature measurement for the SO rather than assuming the same temperature as SO_2.

5. Conclusion

We have presented the first measurements of the combined ^{34}S and ^{33}S isotope ratios relative to ^{32}S in a planet-forming disk. Additionally, we share the upper limit on the $S^{18}O$ column density and the inferred lower limit on the $^{16}O/^{18}O$ ratio. The observed isotopic fractionation of the S reservoir in the Oph-IRS 48 disk is potentially distinct from that measured in comets for both the elements sulfur and oxygen, but this relies heavily on the adopted gas temperature. Assuming a kinetic temperature of 60 K (as measured for SO_2) or above, both ^{34}S and ^{33}S are depleted relative to their solar system standard values when traced in SO. At cooler temperatures, the isotope ratios are consistent with the cometary values, indicating the need for additional data to better and independently constrain the SO gas temperature. Interestingly, at all temperatures the $^{34}S/^{33}S$ ratio traced in SO is enhanced. We also identify a tentative enhancement in the heavier $^{34}SO_2$ isotopologue, which requires observations of optically thinner $^{32}SO_2$ transitions to confirm.

There are also possible limitations in the current data due to dust optical depth that will require longer wavelength observations to assess. It may be that the isotopologues are tracing gas deeper in the disk, below the optically thick dust surface, resulting in an underestimated column density measurement, as seen toward protostars (M. De Simone et al. 2020). Furthermore, follow-up observations with ALMA to detect H_2S (and its isotopologues) will help to complete the observable volatile inventory of S in this disk. Knowing if H_2S is depleted or enhanced in the heavier isotopes will aid significantly in understanding the isotopic fractionation mechanisms at play. More generally, future high-sensitivity line surveys of populations of protoplanetary disks will be able to target multiple isotopologues of S and other volatile elements, which can be used to connect the dots between the initial and final stages of planetary system formation.

Appendix A
$S^{18}O$ Channel Maps

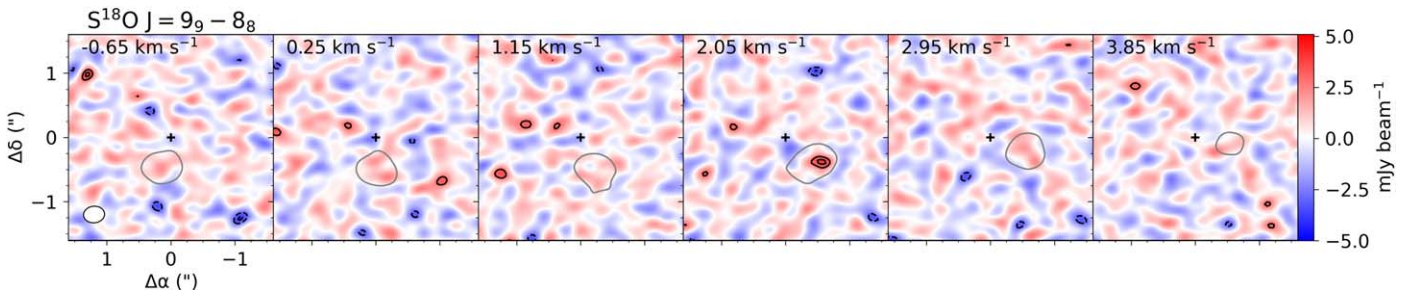The channel maps generated over the frequency range of the $S^{18}O$ $J = 9_9 - 8_8$ transition are shown in Figure A1.

Figure A1. Channel maps of the $S^{18}O$ $J = 9_9 - 8_8$ transition where the black solid contours mark the $[3, 4] \times \sigma$ level and black dashed contours mark $[-4, -3] \times \sigma$ level. The gray solid contour marks the 5σ level of the ^{34}SO $J = 9_8 - 8_7$ transition to show the expected position–velocity pattern of the disk emission.

Appendix B
Isotope Ratios as a Function of Temperature

The isotope ratios of $^{32}S/^{34}S$, $^{32}S/^{33}S$, $^{34}S/^{33}S$, and $^{16}O/^{18}O$ measured from SO and SO_2 as a function of the assumed excitation temperature are shown in Figure B1.

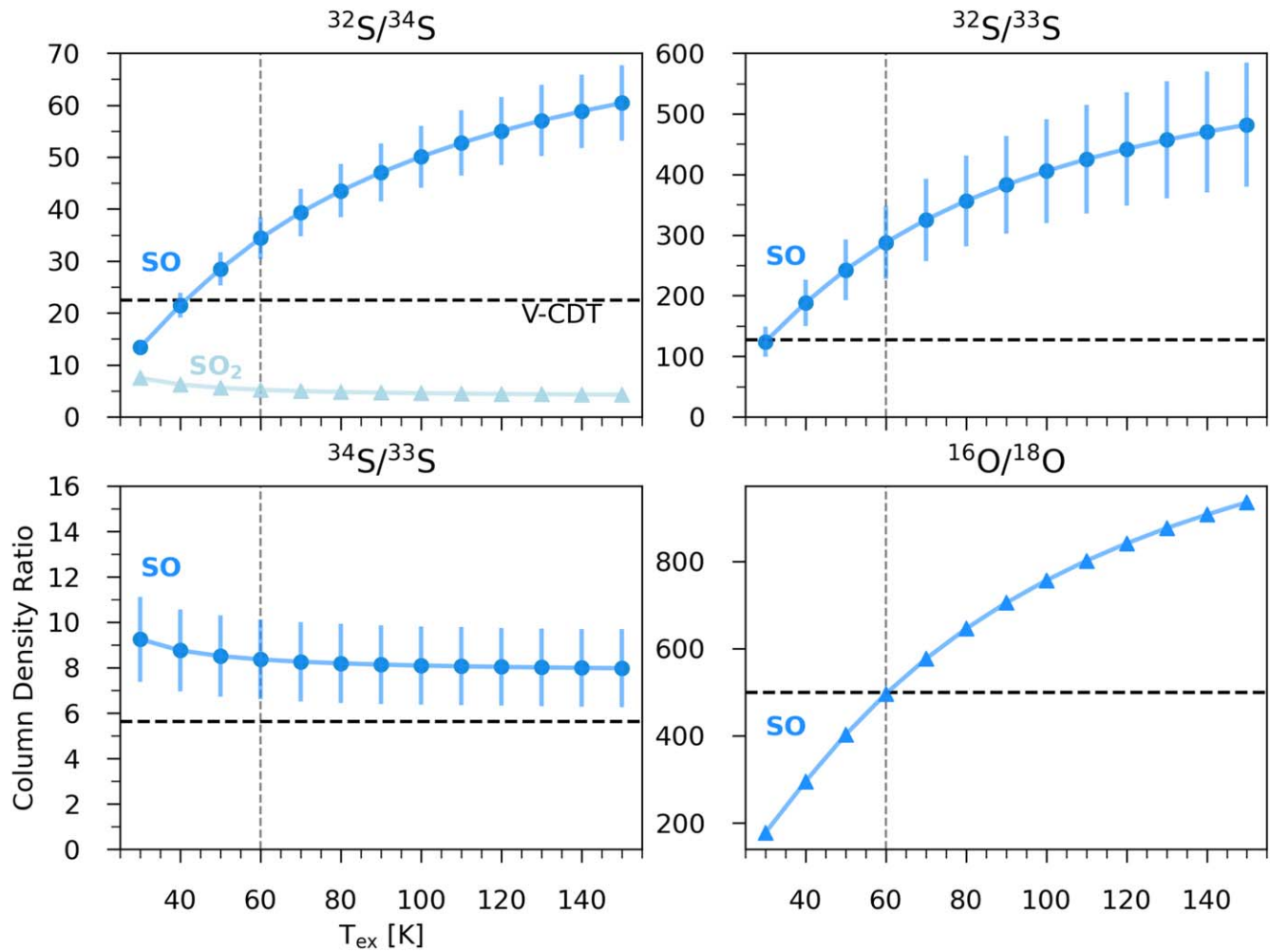**Figure B1.** Inferred isotopic ratios of S and O in SO and SO_2 for the Oph-IRS 48 disk calculated for a range of excitation temperatures. Note the ^{34}S ratio from SO_2 and the ^{18}O ratio from SO are lower limits. The vertical dashed lines highlight our fiducial temperature of 60 K, which is the rotational temperature of SO_2 (Temmink et al. 2024, in preparation). The horizontal dashed lines denote the V-CDT standard isotopic ratios for $^{32}S/^{34}S$, $^{32}S/^{33}S$, $^{34}S/^{33}S$, and $^{16}O/^{18}O$ (R. A. Werner & W. A. Brand 2001; T. Ding et al. 2001).

ORCID iDs

Alice S. Booth ⬥ https://orcid.org/0000-0003-2014-2121
Maria N. Drozdovskaya ⬥ https://orcid.org/0000-0001-7479-4948
Milou Temmink ⬥ https://orcid.org/0000-0002-7935-7445
Hideko Nomura ⬥ https://orcid.org/0000-0002-7058-7682
Ewine F. van Dishoeck ⬥ https://orcid.org/0000-0001-7591-1907
Luke Keyte ⬥ https://orcid.org/0000-0001-5849-577X
Charles J. Law ⬥ https://orcid.org/0000-0003-1413-1776
Margot Leemker ⬥ https://orcid.org/0000-0003-3674-7512
Nienke van der Marel ⬥ https://orcid.org/0000-0003-2458-9756
Shota Notsu ⬥ https://orcid.org/0000-0003-2493-912X
Karin Öberg ⬥ https://orcid.org/0000-0001-8798-1347
Catherine Walsh ⬥ https://orcid.org/0000-0001-6078-786X

References

Aikawa, Y., Furuya, K., Hincelin, U., & Herbst, E. 2018, ApJ, 855, 119
Aikawa, Y., Okuzumi, S., & Pontoppidan, K. 2022, arXiv:2212.14529
Altwegg, K., Balsiger, H., Berthelier, J. J., et al. 2017, RSPTA, 375, 20160253
Altwegg, K., Balsiger, H., Combi, M., et al. 2020, MNRAS, 498, 5855
Artur de la Villarmois, E., Guzmán, V. V., Yang, Y. L., Zhang, Y., & Sakai, N. 2023, A&A, 678, A124
Astropy Collaboration, Price-Whelan, A. M., Lim, P. L., et al. 2022, ApJ, 935, 167
Biver, N., Moreno, R., Bockelée-Morvan, D., et al. 2016, A&A, 589, A78
Booth, A., Leemker, M., van Dishoeck, E. F., et al. 2024, AJ, 167, 164
Booth, A., Temmink, M., van Dishoeck, E. F., et al. 2024, AJ, 167, 165
Booth, A. S., Law, C. J., Temmink, M., Leemker, M., & Macías, E. 2023, A&A, 678, A146
Booth, A. S., van der Marel, N., Leemker, M., van Dishoeck, E. F., & Ohashi, S. 2021, A&A, 651, L6
Brown, J. M., Herczeg, G. J., Pontoppidan, K. M., & van Dishoeck, E. F. 2012, ApJ, 744, 116
Brunken, N. G. C., Booth, A. S., Leemker, M., et al. 2022, A&A, 659, A29
Calmonte, U., Altwegg, K., Balsiger, H., et al. 2016, MNRAS, 462, S253
Calmonte, U., Altwegg, K., Balsiger, H., et al. 2017, MNRAS, 469, S787
Calmonte, U. M. 2015, PhD thesis, Univ. of Bern Switzerland
Cataldi, G., Yamato, Y., Aikawa, Y., et al. 2021, ApJS, 257, 10
Chakraborty, S., Jackson, T. L., Ahmed, M., & Thiemens, M. H. 2013, PNAS, 110, 17650
Crovisier, J., Bockelée-Morvan, D., Colom, P., et al. 2004, A&A, 418, 1141
De Simone, M., Ceccarelli, C., Codella, C., et al. 2020, ApJL, 896, L3
Ding, T., Valkiers, S., Kipphardt, H., et al. 2001, GeCoA, 65, 2433
Drozdovskaya, M. N., van Dishoeck, E. F., Jørgensen, J. K., et al. 2018, MNRAS, 476, 4949
Endres, C. P., Schlemmer, S., Schilke, P., Stutzki, J., & Müller, H. S. P. 2016, JMoSp, 327, 95
Favre, C., Bergin, E. A., Cleeves, L. I., et al. 2015, ApJL, 802, L23
Furuya, K., Tsukagoshi, T., Qi, C., et al. 2022, ApJ, 926, 148
Gaia Collaboration, Brown, A. G. A., Vallenari, A., et al. 2018, A&A, 616, A1
Guzmán, V. V., Öberg, K. I., Huang, J., Loomis, R., & Qi, C. 2017, ApJ, 836, 30

Harris, C. R., Millman, K. J., van der Walt, S. J., et al. 2020, Natur, 585, 357
Heays, A. N., Visser, R., Gredel, R., et al. 2014, A&A, 562, A61
Heck, P. R., Hoppe, P., & Huth, J. 2012, M&PS, 47, 649
Hily-Blant, P., Magalhaes de Souza, V., Kastner, J., & Forveille, T. 2019, A&A, 632, L12
Hily-Blant, P., Magalhaes, V., Kastner, J., et al. 2017, A&A, 603, L6
Holdship, J., Jimenez-Serra, I., Viti, S., et al. 2019, ApJ, 878, 64
Hunter, J. D. 2007, CSE, 9, 90
Jewitt, D. C., Matthews, H. E., Owen, T., & Meier, R. 1997, Sci, 278, 90
Kama, M., Shorttle, O., Jermyn, A. S., et al. 2019, ApJ, 885, 114
Keyte, L., Kama, M., Chuang, K.-J., et al. 2024, MNRAS, 528, 388
Klaus, T., Saleck, A. H., Belov, S. P., et al. 1996, JMoSp, 180, 197
Kluyver, T., Ragan-Kelley, B., Pérez, F., et al. 2016, in Positioning and Power in Academic Publishing: Players, Agents and Agendas, ed. F. Loizides & B. Schmidt (Amsterdam: IOS Press), 87
Kushwhaaa, T., Drozdovskaya, M. N., Tychoniec, Ł., & Tabone, B. 2023, A&A, 672, A122
Labidi, J., Farquhar, J., Alexander, C. M. O. D., Eldridge, D. L., & Oduro, H. 2017, GeCoA, 196, 326
Law, C. J., Booth, A. S., & Öberg, K. I. 2023, ApJL, 952, L19
Le Gal, R., Öberg, K. I., Loomis, R. A., Pegues, J., & Bergner, J. B. 2019, ApJ, 876, 72
Le Gal, R., Öberg, K. I., Teague, R., et al. 2021, ApJS, 257, 12
Leemker, M., Booth, A. S., van Dishoeck, E. F., et al. 2023, A&A, 673, A7
Loomis, R. A., Cleeves, L. I., Öberg, K. I., et al. 2018, ApJ, 859, 131
Loomis, R. A., Öberg, K. I., Andrews, S. M., et al. 2020, ApJ, 893, 101
Lovas, F. J. 1985, JPCRD, 14, 395
Lovas, F. J., Suenram, R. D., Ogata, T., & Yamamoto, S. 1992, ApJ, 399, 325
Marty, B. 2012, E&PSL, 313, 56
McMullin, J. P., Waters, B., Schiebel, D., Young, W., & Golap, K. 2007, in ASP Conf. Ser., 376, Astronomical Data Analysis Software and Systems XVI, ed. R. A. Shaw, F. Hill, & D. J. Bell (San Francisco, CA: ASP), 127
Müller, H. S. P., Schlöder, F., Stutzki, J., & Winnewisser, G. 2005, JMoSt, 742, 215
Müller, H. S. P., Thorwirth, S., Roth, D. A., & Winnewisser, G. 2001, A&A, 370, L49
Muñoz-Romero, C. E., Öberg, K. I., Law, C. J., et al. 2023, ApJ, 943, 35
Nomura, H., Furuya, K., Cordiner, M. A., et al. 2023, in ASP Conf. Ser., 534, ed. S. Inutsuka et al. (San Francisco, CA: ASP), 1075
Öberg, K. I., & Bergin, E. A. 2021, PhR, 893, 1
Öberg, K. I., Facchini, S., & Anderson, D. E. 2023, ARA&A, 61, 287
Ohashi, S., Kataoka, A., van der Marel, N., et al. 2020, ApJ, 900, 81
Paquette, J. A., Engrand, C., Hilchenbach, M., et al. 2018, MNRAS, 477, 3836
Paquette, J. A., Hornung, K., Stenzel, O. J., et al. 2017, MNRAS, 469, S230
Pérez, F., & Granger, B. E. 2007, CSE, 9, 21
Perrero, J., Rimola, A., Corno, M., & Ugliengo, P. 2021, arXiv:2110.06010
Phuong, N. T., Dutrey, A., Chapillon, E., et al. 2021, A&A, 653, L5
Semenov, D., Favre, C., Fedele, D., et al. 2018, A&A, 617, A28
Teague, R. 2020, richteague/keplerian_mask: Initial Release, v1.0, Zenodo, doi:10.5281/zenodo.4321137
Vacher, L. G., Ogliore, R. C., Jones, C., Liu, N., & Fike, D. A. 2021, GeCoA, 309, 135
van der Marel, N., Booth, A. S., Leemker, M., van Dishoeck, E. F., & Ohashi, S. 2021, A&A, 651, L5
Visser, R., Bruderer, S., Cazzoletti, P., et al. 2018, A&A, 615, A75
Werner, R. A., & Brand, W. A. 2001, RCMS, 15, 501
Wilson, T. L., & Rood, R. 1994, ARA&A, 32, 191
Yamato, Y., Notsu, S., Aikawa, Y., et al. 2024, AJ, 167, 66